The Astrophysical Journal Letters, 979:L2 (13pp), 2025 January 20 https://doi.org/10.3847/2041-8213/ad8651

Late-time Radio Brightening and Emergence of a Radio Jet in the Changing-look AGN 1ES 1927+654

Eileen T. Meyer[1], Sibasish Laha[2,3,4], Onic I. Shuvo[1], Agniva Roychowdhury[1,5], David A. Green[6], Lauren Rhodes[7], Amelia M. Hankla[8,9,27], Alexander Philippov[10], Rostom Mbarek[8,9,27], Ari laor[11], Mitchell C. Begelman[12], Dev R. Sadaula[2,3,4], Ritesh Ghosh[2,3,4,13], Gabriele Bruni[14], Francesca Panessa[14], Matteo Guainazzi[15], Ehud Behar[11,16], Megan Masterson[16], Haocheng Zhang[2,3], Xiaolong Yang[17], Mark A. Gurwell[18], Garrett K. Keating[18], David Williams-Baldwin[19], Justin D. Bray[19], Emmanuel K. Bempong-Manful[19,20], Nicholas Wrigley[19], Stefano Bianchi[21], Federica Ricci[21,22], Fabio La Franca[21], Erin Kara[16], Markos Georganopoulos[1], Samantha Oates[23], Matt Nicholl[24], Main Pal[25], and S. Bradley Cenko[2,26]

[1] Department of Physics, University of Maryland, Baltimore County, 1000 Hilltop Circle, Baltimore, MD 21250, USA
[2] Astrophysics Science Division, NASA Goddard Space Flight Center, Greenbelt, MD 20771, USA
[3] Center for Space Science and Technology, University of Maryland, Baltimore County, 1000 Hilltop Circle, Baltimore, MD 21250, USA
[4] Center for Research and Exploration in Space Science and Technology, NASA/GSFC, Greenbelt, MD 20771, USA
[5] Space Telescope Science Institute, 3700 San Martin Dr., Baltimore, MD 21218, USA
[6] Astrophysics Group, Cavendish Laboratory, 19 J.J. Thomson Avenue, Cambridge CB3 0HE, UK
[7] Astrophysics, The University of Oxford, Keble Road, Oxford OX1 3RH, UK
[8] Joint Space-Science Institute, University of Maryland, College Park, MD 20742, USA
[9] Department of Astronomy, University of Maryland, College Park, MD, USA
[10] Department of Physics, University of Maryland, College Park, MD 20742, USA
[11] Department of Physics, Technion, Haifa 32000, Israel
[12] JILA, University of Colorado and National Institute of Standards and Technology, 440 UCB, Boulder, CO 80309-0440, USA
[13] MKHS, Murshidabad, West Bengal, 742401, India
[14] INAF—Istituto di Astrofisica e Planetologia Spaziali, Via del Fosso del Cavaliere 100, Roma 00133, Italy
[15] European Space Agency (ESA), European Space Research and Technology Centre (ESTEC), Keplerlaan 1, 2201 AZ Noordwijk, The Netherlands
[16] Department of Physics & Kavli Institute for Astrophysics and Space Research, Massachusetts Institute of Technology, Cambridge, MA 02139, USA
[17] Shanghai Astronomical Observatory, CAS, 80 Nandan Road, Shanghai 200030, People's Republic of China
[18] Center for Astrophysics | Harvard & Smithsonian, 60 Garden Street, Cambridge, MA 02138, USA
[19] Jodrell Bank Centre for Astrophysics, Department of Physics and Astronomy, The University of Manchester, Manchester M13 9PL, UK
[20] School of Physics, University of Bristol, Tyndall Avenue, Bristol BS8 1TL, UK
[21] Dipartimento di Matematica e Fisica, Università degli Studi Roma Tre, via della Vasca Navale 84, I-00146 Roma, Italy
[22] INAF-Osservatorio Astronomico di Roma, via Frascati 33, 00040 Monteporzio Catone, Italy
[23] Birmingham Institute for Gravitational Wave Astronomy and School of Physics and Astronomy, University of Birmingham, Birmingham B15 2TT, UK
[24] Astrophysics Research Centre, School of Mathematics and Physics, Queens University Belfast, Belfast BT7 1NN, UK
[25] Department of Physics, Sri Venkateswara College, University of Delhi, Benito Juarez Road, Dhaula Kuan, New Delhi—110021, India
[26] Joint Space-Science Institute, University of Maryland, College Park, MD 20742, USA
Received 2024 June 24; revised 2024 October 11; accepted 2024 October 13; published 2025 January 13

Abstract

We present multifrequency (5–345 GHz) and multiresolution radio observations of 1ES 1927+654, widely considered one of the most unusual and extreme changing-look active galactic nuclei (CL-AGNs). The source was first designated a CL-AGN after an optical outburst in late 2017 and has since displayed considerable changes in X-ray emission, including the destruction and rebuilding of the X-ray corona in 2019–2020. Radio observations prior to 2023 show a faint and compact radio source typical of a radio-quiet AGN. Starting in 2023 February, 1ES 1927+654 began exhibiting a radio flare with a steep exponential rise, reaching a peak 60 times previous flux levels, and has maintained this higher level of radio emission for over a year to date. The 5–23 GHz spectrum is broadly similar to gigahertz-peaked radio sources, which are understood to be young radio jets less than ∼1000 yr old. Recent high-resolution Very Long Baseline Array observations at 23.5 GHz now show resolved extensions on either side of the core, with a separation of ∼0.15 pc, consistent with a new and mildly relativistic bipolar outflow. A steady increase in the soft X-ray band (0.3–2 keV) concurrent with the radio may be consistent with jet-driven shocked gas, though further observations are needed to test alternate scenarios. This source joins a growing number of CL-AGNs and tidal disruption events that show late-time radio activity, years after the initial outburst.

Unified Astronomy Thesaurus concepts: Radio jets (1347); Active galactic nuclei (16); Proper motions (1295); X-ray active galactic nuclei (2035); Radio active galactic nuclei (2134); Seyfert galaxies (1447)

1. Introduction

Recent advances in time-domain studies have led to the identification of new types of extreme variability in active galaxies, popularly called "changing-look" active galactic nuclei (CL-AGNs). These extreme variations are characterized not only by orders-of-magnitude changes in the optical, UV, and X-ray luminosity of the source but also by an unexpected

[27] Neil Gehrels Fellow.

transition between optical spectral types (S. Mathur et al. 2018; B. Trakhtenbrot et al. 2019; M. Kokubo & T. Minezaki 2020; S. Komossa et al. 2020). In the simplest AGN unification framework, those with broad emission lines (type 1) are thought to be viewed more face-on, such that the central nucleus is unobscured, while type 2 AGNs are thought to be viewed at higher inclination angles, in which case an inferred dusty torus obscures the broad-line-emitting clouds, resulting in only narrow optical emission lines in the optical spectrum (R. Antonucci 1993; S. Bianchi et al. 2012; C. R. Almeida & C. Ricci 2017). While we have long known that many factors complicate this simple picture (e.g., strength of the central continuum, variations in the amount and distribution of molecular gas and dust), the drastic changes seen in CL-AGNs in such short timescales (a few weeks to months) challenge the simplest form of the AGN unification framework, which has generally assumed that such changes occur over far longer timescales (see C. Ricci & B. Trakhtenbrot 2023, for a recent review).

The AGN 1ES 1927+654 ($z = 0.017$; 348 pc arcsec^{-1}) is widely considered one of the most unusual and extreme CL-AGNs yet discovered (B. Trakhtenbrot et al. 2019; C. Ricci et al. 2020, 2021; S. Laha et al. 2022; M. Masterson et al. 2022; R. Ghosh et al. 2023) and is one of the extremely few CL-AGNs observed to change in real time. Earlier X-ray and optical observations of 1ES 1927+654 classified it as a "true" or "naked" type 2 AGN, with no evidence for obscuration by dust along the line of sight to explain the lack of broad emission lines (T. Boller et al. 2003; H. D. Tran et al. 2011). It was first flagged as a transient source of significantly increasing flux by the All-Sky Automated Survey for Supernovae (ASAS-SN; B. J. Shappee et al. 2014) program on 2018 March 3 (ASAS-SN-18el/AT2018zf; B. Nicholls et al. 2018). In the original discovery paper, B. Trakhtenbrot et al. (2019) used archival data from the Asteroid Terrestrial-impact Last Alert System (J. L. Tonry et al. 2018) to show that the outburst actually began in 2017 December and that the total increase was nearly 5 mag in the *V* band (a factor of 100 in total flux). An initially nearly featureless optical quasar spectrum began to show increasing broad lines approximately 70−90 days after the peak in the optical band, which occurred in 2018 March. The broad-line fluxes continued to increase in strength out to roughly 150 days after the continuum peak and persisted for at least 11 months after the optical flare. This behavior follows the expectations for the illumination of a previously existing broad-line region of size ∼1−3 light-months.

Subsequent to the initial CL outburst, the source has displayed a series of unusually varied states in the X-ray band while showing no change other than a monotonic return to pre-CL values in the optical/UV and general quiescence in the radio (up to the currently reported outburst). After a short period of X-ray emission similar to pre-CL levels, the 2–10 keV hard X-ray emission (i.e., the corona) completely vanished for about 3 months in 2018 before flaring up by a factor 1000 to exceed the Eddington limit for a $10^6\,M_\odot$ black hole (BH; C. Ricci et al. 2020), a state it maintained for over a year before dropping back to pre-outburst levels (C. Ricci et al. 2021; M. Masterson et al. 2022).

While the initial optical/UV flare and decay timescale appears consistent with a possible tidal disruption event (TDE) in an existing AGN, the X-ray spectral changes are not, including both short- and long-term variability and temperature variations for the thermal X-ray component in the first few years after the CL event (M. Masterson et al. 2022). One possibility is that the CL event was the result of a magnetic flux inversion event in a magnetically arrested disk (N. Scepi et al. 2021). This could explain the much shallower UV flux decay than expected under a TDE, the X-ray minimum following the outburst, and the lack of TDE-like spectral features (S. Laha et al. 2022). Most recently, R. Ghosh et al. (2023) have reported the emergence of a new bright and soft X-ray component in 1ES 1927+654 (along with an undiminished X-ray corona), which began in late 2022 and continues up to the present epoch. It was this enhanced state that triggered a director's discretionary time (DDT) request to the Very Long Baseline Array (VLBA), which led to the fortunate timing of much of the radio monitoring presented here.

2. Observation

2.1. Overview of Past and Present Radio Monitoring

The source 1ES 1927+654 has been observed in the radio with the Very Large Array (VLA) and VLBA on only a few occasions prior to the CL event. E. S. Perlman et al. (1996) report a flux density of 16 mJy at 6 cm measured by the VLA in CnB hybrid configuration with a resolution of approximately 5″. Observations with the VLBA taken in 2013 and 2014 (previously published in S. Laha et al. 2022) are included here for comparison to more recent data. Post-CL event, the source was observed by the VLBA once at *C* band in 2018 December and then sporadically with both the VLBA and European VLBI Network (EVN) on timescales of 6–12 months from 2020 January by our group and others. This longer-timescale monitoring was primarily motivated by the months-long-timescale X-ray changes seen by Swift and NICER, to look for possible correlated radio variability.

While our standard monitoring observations with the VLBA at 5 GHz showed no major change between 2022 March and August (total flux of 6 and 5 mJy, respectively), we made a DDT request in 2023 April (BR256) based on the soft X-ray flux seen by Swift, which had been steadily rising since late 2022. This observation resulted in the surprising finding that the *C*-band (5 GHz) flux density had increased by a factor of 7 to 37.4 mJy. We immediately triggered additional DDT requests to the VLBA, EVN, VLA, the Arcminute Microkelvin Imager (AMI), e-MERLIN, and the Submillimeter Array (SMA) from 2023 April up to the time of this Letter, on timescales ranging from every few days to monthly. As of 2024 May, the source is still being monitored regularly by the VLBA, EVN, and e-MERLIN. In this initial publication, we present primarily the VLBA and EVN observations of 1ES 1927+654 to date, as well as the observations by AMI, one of the several VLA observations obtained in 2023 May, and millimeter-band measurements by the SMA in 2023 July and 2024 June.

2.2. VLBA Calibration and Imaging

The VLBI observations spanning 2013 to early 2024 are summarized in Table 1, where we describe both the VLBA observations and those from the EVN, discussed in the next section. In particular, we give the observation date, program name, central frequency in GHz, and the final image rms value in mJy beam^{-1} in Columns (1)–(5). In Columns (6) and (7) we give the peak radio flux in mJy beam^{-1} and the total radio flux of the source in mJy. The restoring beam (i.e., approximately the resolution of the imaging) is given in Column (8) as the

Table 1
VLBA and EVN Observation and Radio Properties

Date	Segment	Band	Freq. (GHz)	rms (mJy beam^{-1})	$F_{\rm peak}$ (mJy bm^{-1})	$S_{\rm tot}$ (mJy)	Rest. Beam ($\alpha \times \delta$; mas)	Beam Angle (deg)	Self-calibration
(1)	(2)	(3)	(4)	(5)	(6)	(7)	(8)	(9)	(10)
				Previously Published					
2013-08-10	EG079A[a]	L	1.48	0.25	⋯	18.9	28.2 × 11.7	⋯	⋯
2014-03-25	EG079B[a]	C	4.99	0.03	3.6[b]	4.1	2.47 × 1.18	⋯	⋯
2018-12-04	RSY07[a]	C	4.99	0.04	0.7[b]	8.4	6.01 × 4.95	⋯	⋯
				New Observations					
2020-01-17	BY149	S	2.28	0.15	1.78	3.99	6.4 × 3.3	0.95	no
		X	8.43	0.03	0.26	1.61	1.7 × 1.0	5.46	no
2021-03-15	BM518	C	4.98	0.04	1.33	5.32	3.9 × 1.5	15.82	no
2022-03-05	BM527	C	4.87	0.04	2.95	5.89	3.8 × 2.5	28.98	no
		X	8.37	0.03	1.20	2.38	2.2 × 1.2	22.59	no
2022-08-05	BY177B	C	4.87	0.03	1.89	4.95	4.0 × 1.6	17.88	no
2022-08-08	BY177C	X	8.37	0.02	1.10	1.83	1.6 × 0.9	−4.23	no
2023-02-10	BY177F	X	8.37	0.03	10.57	11.92	1.7 × 1.0	−11.48	p
2023-02-18	BY177E	C	4.87	0.21	6.84	8.26	4.3 × 2.0	13.46	p
2023-04-27	BR256	C	4.98	0.05	36.32	37.47	3.9 × 1.5	−5.15	a+p
		X	8.42	0.05	47.09	48.77	2.3 × 0.9	−8.06	a+p
2023-05-21	BM549A	C	4.98	0.07	48.44	49.74	3.9 × 1.4	−4.15	a+p
		X	8.42	0.04	39.79	40.61	2.3 × 0.9	−6.76	a+p
2023-05-28	BM549B	C	4.98	0.05	53.33	55.92	4.1 × 1.5	−4.15	a+p
		X	8.42	0.07	45.91	47.32	2.5 × 1.0	−5.80	a+p
2023-06-01	BM549C	C	4.98	0.05	67.36	67.60	3.9 × 1.6	−9.18	a+p
		X	8.42	0.05	50.11	51.76	2.3 × 0.8	−9.94	a+p
2023-06-08	BM549D	C	4.98	0.10	69.27	73.10	4.0 × 1.8	20.75	a+p
		X	8.42	0.13	57.22	58.58	2.2 × 0.8	23.17	a+p
		K	22.22	0.11	20.69	20.91	0.9 × 0.4	19.07	a+p
2023-06-28	RB008[a]	C	4.93	0.08	55.59	54.58	9.2 × 2.7	−85.89	a+p
2023-07-22	BM550A	C	4.87	0.07	58.42	63.82	4.0 × 1.8	−22.15	a+p
		X	8.37	0.10	59.42	61.29	2.4 × 1.0	−25.01	a+p
		K	23.55	0.21	10.90	13.05	0.8 × 0.4	−31.35	no
2023-08-31	BM550B	C	4.87	0.12	52.06	54.31	3.6 × 1.3	−19.58	a+p
		X	8.36	0.07	53.85	55.65	2.3 × 0.8	−23.72	a+p
		K	23.57	0.30	5.66	5.27	0.9 × 0.3	−27.93	no
2023-09-23	BM550C	C	4.87	0.12	62.26	65.50	4.6 × 1.6	−15.75	a+p
		X	8.36	0.11	52.07	54.55	2.8 × 0.9	−17.57	a+p
		K	23.57	0.30	5.06	6.30	1.0 × 0.4	−22.25	no
2023-10-22	EY038A[a]	X	8.41	0.06	44.53	47.51	1.5 × 0.5	−44.84	a+p
2023-10-26	EY038B[a]	L	1.66	0.05	32.67	45.81	15.9 × 3.1	−47.47	a+p
2023-10-27	BM550D	C	4.87	0.06	64.73	65.07	4.3 × 2.0	−26.28	a+p
		X	8.36	0.06	50.88	54.50	2.5 × 1.0	−25.48	a+p
		K	23.57	0.24	7.45	19.50	0.9 × 0.6	27.04	no
2023-11-01	EY038C[a]	C	4.93	0.03	48.20	51.07	4.2 × 2.7	32.38	a+p
2023-11-09	RB009[a]	K	22.24	0.50	9.16	10.45	0.7 × 0.2	9.22	no
2023-11-26	BM550E	C	4.87	0.07	54.60	59.66	4.1 × 1.9	−20.92	a+p
		X	8.37	0.20	45.31	46.68	2.3 × 0.8	−21.00	a+p
		K	23.57	0.07	13.12	15.86	0.9 × 0.4	−23.83	a+p
2023-12-26	BM550F	C	4.87	0.08	64.82	69.02	4.4 × 1.5	−21.44	a+p
		X	8.37	0.07	48.99	51.40	2.6 × 0.8	−24.06	a+p
		K	23.57	0.12	9.93	14.77	0.9 × 0.4	−32.18	p
2024-02-09	BM556A	C	4.87	0.06	69.64	74.36	3.0 × 2.0	−33.80	a+p
		X	8.37	0.05	47.42	50.44	1.8 × 1.1	−31.59	a+p
		K	23.57	0.11	8.15	10.53	0.7 × 0.5	−43.13	p
2024-03-12	EB106[a]	K	22.24	0.16	6.16	7.09	1.0 × 0.7	−7.68	no
2024-04-24	BM556B	C	4.87	0.08	69.30	74.47	4.6 × 1.4	−0.47	a+p
		X	8.37	0.05	54.04	57.97	2.7 × 0.9	−6.84	a+p
		K	23.57	0.14	17.10	19.52	0.9 × 0.4	−11.61	p
2024-05-30	BM556C	L	1.63	0.36	29.60	36.50	9.2 × 4.3	−28.70	a+p
		C	4.87	0.29	74.72	77.23	3.3 × 1.6	−20.75	a+p
		X	8.37	0.12	61.36	66.42	1.9 × 0.9	−24.68	a+p
		K	23.57	0.06	19.88	24.38	0.8 × 0.4	−24.15	p

Notes. Previously published observations (top three entries) taken from S. Laha et al. (2022).
[a] Observed by the EVN.
[b] Fluxes were reported as central point-source flux densities.

semimajor and minor ellipse axis length in mas, and the orientation of the ellipse in degrees is given in Column (9). The final column notes whether self-calibration was possible for the imaging ("no" indicates that it was not, "p" indicates that phase-only self-calibration was applied, and "ap" indicates both amplitude and phase).

For those observations with sufficient signal-to-noise ratio (SNR) per antenna for reasonable short solution intervals, we applied one or more iterations of phase-only self-calibration. In some cases the SNR was insufficient to proceed further, while in others (most *C*- and *X*-band observations) a single additional amplitude and phase self-calibration was applied. We verified that any self-calibration applied resulted in improved image rms, and the values reported in Table 1 correspond to the self-calibrated image where this is the case.

In the initial calibration of all VLBA observations, we utilized the National Radio Astronomy Observatory (NRAO) Astronomical Image Processing System, also known as AIPS (G. van Moorsel et al. 1996). Specifically, we used the new primary development version of AIPS, release 31DEC23. Each frequency data set was calibrated independently by pairing the target source with the phase calibrator (J1933+6540). We followed standard calibration procedures using VLBAUTIL and flagged bad data when necessary. We completed the calibration process for the phase calibrator and applied the calibrations to the source using the SPLIT task. Once these standard AIPS calibration procedures were finished, we proceeded to the imaging stage. We utilized the IMAGR task in AIPS to create images of both the calibrators and sources.

We also utilized the NRAO Common Astronomical Software Applications (CASA; CASA Team et al. 2022)[28] to analyze images from our VLBA observations. To determine the integrated flux densities for sources, we used the two-dimensional fitting application through the VIEWER command in CASA. In Table 1, we listed the flux density values for all of our observations, along with all the radio properties of the final images.

In the three most recent *K*-band VLBA observations (2024 February 9, April 24, and May 30), resolved components were apparent in the residual images after the initial core was subtracted during the CLEAN deconvolution (further discussed in Section 3.2). A more extensive investigation into the source structure at all bands (and complimented by the necessary observation simulations to provide better estimates of systematic errors) is planned for a future publication, but we do present some initial results here, focusing on the highest-resolution *K*-band data. In order to measure the flux and position of the resolved components, we produced core-subtracted measurement sets and images. Beginning in each case from the original data with one round of phase-only self-calibration applied, we used a small clean box region of only a few-pixel extent over the core region to produce a point-source model in the measurement set corresponding to the core emission only,[29] stopping at the same residual flux level (approximately 0.19 mJy beam^{-1}) in the central core region. For comparison, we also produced a core-subtracted image for the 2023 June observation, continuing to the level of the image rms (since no residual emission was apparent). The core emission was then subtracted using the CASA task `uvsub`, before reimaging the resulting measurement set. We utilized `DIFMAP` (M. C. Shepherd 1997) on the core-subtracted *K*-band visibility data from the 2024 *K*-band epochs to test the presence of true extended emission. All of the epochs were consistent, to first order, with a dual point-source structure located on opposite sides of the core location. The evolution of the flux densities and the positions of the point sources have been noted in Table 2, along with the separation between the two point sources.

2.3. EVN Calibration and Imaging

The EVN epochs performed between 2023 and 2024 are summarized in Table 1. Phase-referencing was performed, adopting the same calibrator as for the VLBA observations (J1933+6540, at a separation of $\sim 0.^{\circ}7$). For the first epoch (RB008, *C* band) participating antennas were Jb, Wb, Ef, Mc, Nt, O8, T6, Tr, Hh, Ys, and Ib, while the later epochs at higher frequency (RB009 and EB106, *K* band) could count on the participation of the Korean VLBI Network (KVN) adding sensitivity to the longest baselines. Participating antennas were Jb, Ef, Mc, O6, T6, Ur, Tr, Mh, Kt, Ky, Ku and Jb, Ef, Mc, O6, T6, Ur, Tr, Mh, Ys, Sr, Kt, Ky, Ku, respectively. Further information and observation logs are available at the EVN archive (https://archive.jive.nl/scripts/portal.php). Raw data from single antennas were correlated at the Joint Institute for VLBI ERIC (JIVE, Dwingeloo). Calibration was performed in `CASA`, through the `rPICARD` pipeline (M. Janssen et al. 2019). The calibrated visibilities were then imaged with `DIFMAP` (M. C. Shepherd 1997), following a standard phase and amplitude self-calibration procedure. Finally, integrated flux densities were extracted via a two-dimensional Gaussian fitting in `CASA`.

Three additional EVN epochs, EY038A (observed on 2023 October 22), EY038B (2023 October 26), and EY038C (2023 November 1), were obtained from the PI (X. Yang) after our initial analysis of the above-referenced data. These observations followed similar phase-referencing techniques with the same calibrator J1933+6540. The antennas involved were as follows: EY038A included WB, EF, MC, O6, T6, UR, TR, IB, and WZ; EY038B included JB, WB, EF, MC, O8, T6, UR, TR, and IR; and EY038C included JB, WB, EF, MC, O8, T6, UR, TR, IB, and SR. Calibration followed the procedures outlined in the EVN data reduction guide (https://www.evlbi.org/evn-data-reduction-guide), with imaging and self-calibration carried out similarly to the other EVN and VLBA observations.

2.4. Very Large Array C-band Observations

In the high-cadence VLA observing program 23A-407, our source was observed 11 times between May 20 and June 1. Here we present the observations of 2023 May 21, which were contemporaneous with a VLBA observation, to put limits on the large-scale radio flux, which may contaminate lower-resolution observation (such as with AMI), and to measure the degree of polarization in the radio, if any. A full presentation of the remaining VLA observations will be made in a forthcoming paper.

For the 2023 May 21 observations the array was in B configuration and we used a standard 8-bit *C*-band continuum observing setup with 2048 MHz bandwidth. Radio frequency interference (RFI) losses resulted in a reduction of bandwidth by an estimated 15%–20% on most baselines and the complete loss of spectral window 10. 3C 48 served as the primary bandpass and flux calibrator, as well as the polarization calibrator for the cross-hand delay and polarization angle, using values from 2019 available from the NRAO website (see, e.g., R. A. Perley & B. J. Butler 2017). The unpolarized source

[28] https://casa.nrao.edu

[29] From the variability timescale we know that the central source, which is responsible for the fast rise, is very small, well below the VLBA imaging resolution and thus appropriately modeled as a point source; typical point-source localization accuracy is on the order of a few to tens of microarcseconds.

Table 2
Results of DIFMAP Fitting to Resolved Components in *K*-band Imaging

Observation	Decimal Date	Component	Flux[a] (mJy)	δ East (μas)	δ North (μas)	Separation (mas)	P.A. (deg)
(1)	(2)	(3)	(4)	(5)	(6)	(7)	(8)
BM556A	2024.107	core	7.66	…	…	…	…
		NE	1.88 ± 0.03	88 ± 4	218 ± 5	0.40 ± 0.01	23 ± 1
		SW	1.87 ± 0.03	-70 ± 4	-146 ± 5		
BM556B	2024.311	core	15.1	…	…	…	…
		NE	2.26 ± 0.05	135 ± 7	173 ± 32	0.45 ± 0.05	24 ± 4
		SW	2.23 ± 0.05	-47 ± 7	-242 ± 32		
BM556C	2024.41	core	14.0	…	…	…	…
		NE	4.70 ± 0.05	164 ± 2	284 ± 3	0.50 ± 0.01	31 ± 1
		SW	3.51 ± 0.03	-93 ± 2	-142 ± 3		

Notes. The quoted errors are the formal 1σ values from the fitting and do not account for systematic effects.
[a] The flux listed for the core in each epoch is the value used in the core subtraction.

J2355+4950 was used to determine instrumental polarization (leakage/D-terms), and J1927+6117 was used as a secondary gain calibrator. All calibration, imaging, and analysis was carried out with the CASA package. We used a modified version of the CASA pipeline (6.5.4.9) for the initial calibration and then determined the polarization calibration tables by hand after additional flagging of both source and calibrators for RFI. In the initial pipeline run we ran the `hifv_syspower` task with `apply=True` to counteract the effects of gain compression due to strong RFI. The CASA task `tclean` was used in interactive mode for imaging deconvolution using standard wide-band continuum parameters (mtmfs deconvolver with nterms = 2, natural weighting). Two rounds of self-calibration were applied after initial imaging of Stokes *I* only, one phase-only followed by a cumulative amplitude+phase table. The final full-Stokes (*IQUV*) imaging used natural weighting with a pixel scale of $0\farcs1$. The resulting images have a restoring beam of $1\farcs6 \times 1\farcs2$ oriented at $-4\fdg25$. The Stokes *I*, *Q*, *U*, and *V* images have rms values of $(2.5,\ 2.1,\ 2.4,\ 2.2) \times 10^{-5}$ Jy beam^{-1}, respectively.

The resulting total intensity map of 1ES 1927+654 shows an unresolved point source of 53 mJy (reference frequency 5.5 GHz) with very low to zero polarization. The flux density is consistent with the VLBA flux density measurement of 49 mJy at 4.98 GHz on the same date given typical uncertainties on the absolute flux density scale of ∼5%–10%. The linear polarization intensity map formed from the Stokes *Q* and *U* images is shown in Figure 1 and shows a point source with peak flux density 0.29 mJy, which is approximately 7 times the (polarized intensity) image rms. However, similar low-level peaks that are clearly noise can be seen in several locations in the image, with peak levels up to ∼0.1 mJy. The peak of polarized intensity is also not perfectly aligned with the peak in the Stokes *I* image. Thus, some caution is warranted, and we interpret this as an upper limit of 0.6% on the linear polarization fraction at *C* band. The Stokes *V* image does not show any signs of an excess, and based on the *V*-band rms, we report an upper limit of 0.2% on the circular polarization.

2.5. Arcminute Microkelvin Imager Observations at 15.5 GHz

1ES 1927+654 was observed on many occasions between 2023 June 7 and 2024 April 2 with the Large Array of AMI (J. T. L. Zwart et al. 2008; J. Hickish et al. 2018). AMI consists of eight 12.8 m antennas sited at the Mullard Radio Astronomy Observatory near Cambridge, UK. The AMI receivers cover the band from 13 to 18 GHz and are of a single linear polarization, Stokes *I*+*Q*. We report here 58 observations taken over the above time frame with a mean spacing of ∼5.3 days. Analysis was done using custom software, REDUCE_DC (Y. C. Perrott et al. 2013). Each observation consisted of multiple 10-minute scans of 1ES 1927+654, interleaved with short (∼2-minute) observations of a nearby compact source, which were used for phase calibration. The flux density scale was set using nearby observations of 3C 286, which were usually made daily. The number of antennas available varied between observations, due to technical issues, and usually longer observations were made when there were fewer working antennas available. The day-to-day flux density uncertainty is estimated at ∼5%.

2.6. e-MERLIN

Regular observations from e-MERLIN cycle 16 program CY16025 were obtained as "filler" scans at *C* band inserted into other accepted programs using that frequency. Partial results from this program, namely data from 2023 September to November, so far have been made available as fully calibrated uvfits files. With only modest "snapshot" depth observations, the UV coverage is not always sufficient for reliable imaging deconvolution, so we have opted for a nonimaging analysis method to obtain the source flux in the e-MERLIN observations. In particular, we use the CASA task `uvmodelfilt` to fit a simple point-source model to the visibilities, adjusting the starting values to ensure stability and convergence. The model column of the measurement set file is then populated according to the fit results, and we apply standard self-calibration cycles with decreasing solution intervals to then improve the applied calibration, rerunning the model fit at each step. We conducted several rounds of phase-only (noncumulative) self-calibration followed by a single round of amplitude and phase calibration. In the middle panel of Figure 2, we show the preliminary results from this program, as three data points corresponding to roughly weekly averages.

2.7. Submillimeter Array

The source 1ES 1927+654 was observed twice by the SMA in Hawaii, on 2023 July 31 and 2024 June 11 (hereafter epochs 1 and 2, respectively). In both observations there were six SMA antennas operating in similar compact configurations with

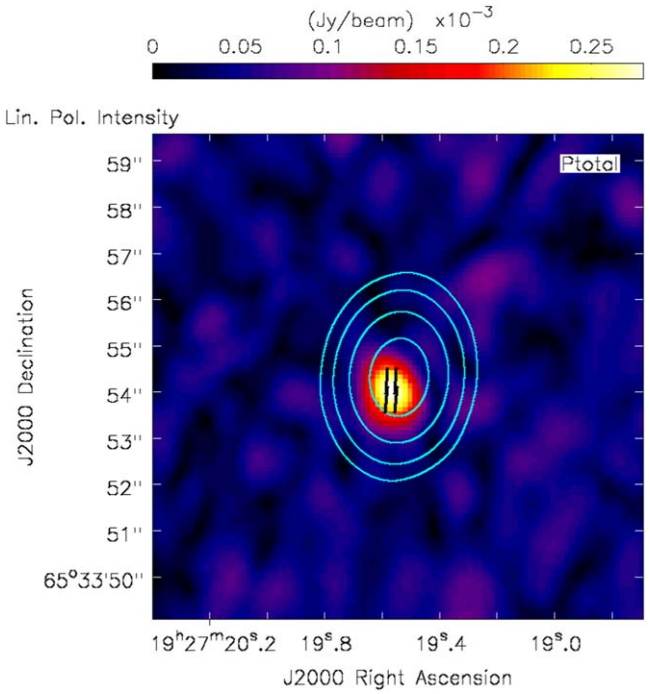

Figure 1. Total polarized intensity map at 5.5 GHz for the VLA observation of 2023 May 21. The color scale gives the flux density in mJy beam^{-1}. Contours overlaid in cyan correspond to the total (Stokes *I*) intensity, with levels at 10, 50, 250, and 1000 times the base value 2.5×10^{-5} Jy beam^{-1}, which is approximately the total intensity image rms. The vectors shown in black correspond to the measured linear polarization EVPA (no rotation applied). The polarized intensity peak appears slightly offset from the total intensity peak and has a value of 0.29 mJy, corresponding to a 0.6% polarization fraction.

baselines up to ∼80 m. In epoch 1 the target was observed in a single frequency band using two orthogonally polarized double-sideband receiver sets, each processing 12 GHz of bandwidth per sideband (providing a total of 48 GHz of processed bandwidth) centered at a frequency of 225.5 GHz ($\lambda \sim 1.35$ mm). In epoch 2 the observation included simultaneous dual-band observations, each with a single polarization (providing 24 GHz of processed bandwidth each), one again centered at 225.5 GHz and the other at 347 GHz ($\lambda \sim 870\ \mu$m). The weather was very good in both observations, with the water vapor column ranging between 1.5 and 2 mm precipitable water vapor. Observations of 1ES 1927+654 were interleaved with observations of nearby gain calibration sources, J1806+698 and J1927+739, with the absolute flux scale calibrated primarily against the continuum of MWC 349A, with added checking in epoch 1 using Ceres and Callisto. Standard reduction using the SMA MIR calibration suite was performed for both epochs 1 and 2.[30] The data for epoch 2 were also processed using the COMPASS pipeline reduction package, which provides several improved and automated steps for data flagging and quality control (G. K. Keating 2024, private communication). The total usable on-source integration time was 7.13 and 6.97 hr for epochs 1 and 2, respectively. The synthesized spatial resolution at 225.5 GHz was similar for both epochs, $\sim 3\farcs0 \times 3\farcs0$, while the higher frequency band in epoch 2 at 347 GHz achieved a resolution of $2\farcs2 \times 1\farcs9$. For epoch 1 (225.5 GHz), the flux density was found to be 5.49 ± 0.29 mJy, determined from a vector average of the calibrated visibility data, and confirmed using imaging using the AIPS task IMAGR. For epoch 2, the flux density at 225.5 GHz was measured to be 5.73 ± 0.35 mJy (consistent with epoch 1), and at 347 GHz the flux density was 4.57 ± 1.27 mJy using the COMPASS pipeline reduction and imaging path.

[30] https://lweb.cfa.harvard.edu/rtdc/SMAdata/process/mir/

3. Results and Discussion

3.1. Radio Light-curve and SED Evolution

In Figure 2 we show the main result for 1ES 1927+654, which is a ∼40- and 60-fold increase at 5 and 8.4 GHz in the core radio flux density over a very short time period from 2023 January to June. The top panel shows the 0.3–2 keV soft X-ray flux as seen by Swift/XRT for comparison (see S. Laha et al. 2024 for further details). The middle panel shows the total radio flux in the VLBA observations at 5.4, 8.4, and 22.2/23.5 GHz (*C*, *X*, and *K* bands), as well as fluxes from lower-resolution instruments e-MERLIN (5 GHz) and AMI (15.5 GHz). The 5–8.4 GHz and 8.4–23 GHz spectral indices are shown in the bottom panel over the same time frame. The peak radio flux was likely reached between the June 8 and July 22 epochs of VLBA monitoring, in agreement with the peak in the AMI light curve on June 27. The 5.4–8.4 GHz spectral index became notably "flat" ($\alpha < 0.5$ for $\nu^{-\alpha}$) during the fast rise in early 2023 and has remained so in nearly all epochs in the year following. The radio-loudness is now $R \approx 100$, where R is the ratio of the optical (traditionally *B*-band) flux to that in the radio at 5 GHz. We use the recent consistent quiescent optical magnitude of $m_g = 17$ as seen by the Zwicky Transient Facility (ZTF; F. J. Masci et al. 2019), equivalent to a flux of ∼0.6 mJy for the optical flux density. The source can thus be argued to now be radio-loud, though the dividing line between radio-quiet, radio-intermediate, and radio-loud is debated (e.g., H. Falcke et al. 1996)

The near-weekly cadence of VLBA observations in 2023 May–June fortunately caught the source during the exponential rise phase. A fit to the six *C*-band observations from 2023 February 18 to June 8 with an exponential function gives a characteristic timescale of ∼44 days, with an equivalent light-crossing size limit of about 0.04 pc (assuming no significant beaming). This is just below the resolution of our *K*-band VLBA imaging, which has a synthesized beam on the order of 0.4–0.8 mas or 0.15–0.30 pc. In the nearly 1 yr since the radio outburst began, the source has maintained near-peak radio luminosity with only low-level variability from 5 to 15.5 GHz.[31] The average 5.4 GHz flux density of 65 mJy since the peak in 2023 June corresponds to a radio power of $\nu L_{\nu,\mathrm{R}} = 2.6 \times 10^{39}$ erg s^{-1}.

The VLBI-resolution radio spectral energy distribution from 2020 January to 2024 April ($\log F_\nu$ vs. $\log \nu$) is shown in Figure 3, where we plot the total flux density. The spectrum is notably curved with a peak at or just below 5 GHz with an appearance similar to gigahertz-peaked spectrum (GPS) AGN sources, as further discussed below. We also include in this figure SMA observations from 2024 June, at 225 and 345 GHz (the 2023 July observation at 225 GHz only resulted in an

[31] The 22.2–23.6 GHz *K*-band flux shows a somewhat higher degree of variability, but we strongly suspect that some of the early *K*-band observations with quite low fluxes compared to the rest were affected by decoherence losses due to a less ideal phase calibrator (BM550A-D observations in particular). In some of these epochs we also were not able to self-calibrate at *K* band. We adopt a larger error bar of 30% vs. a standard 10% for the non-self-calibrated epochs in Figure 2).

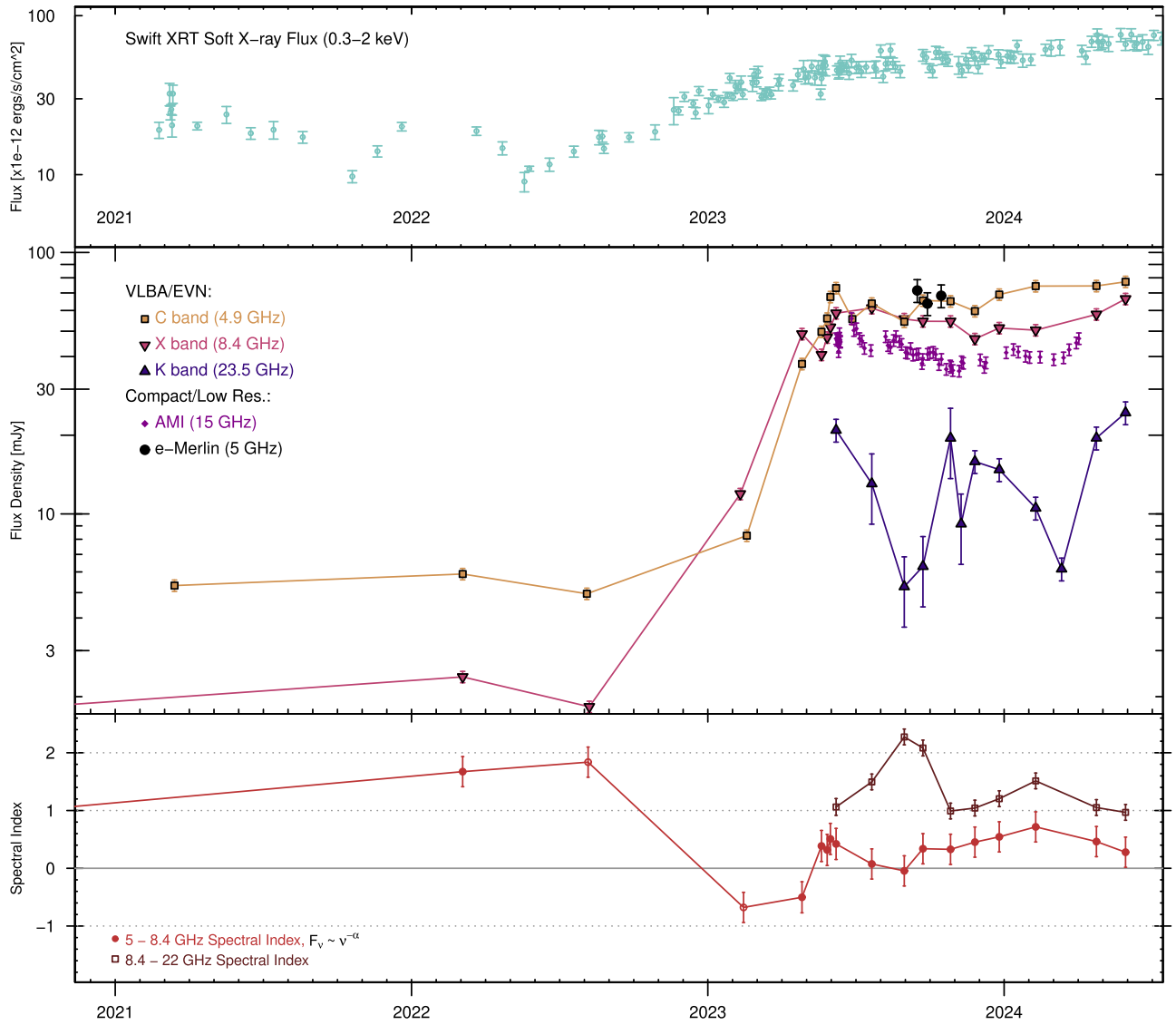

Figure 2. The soft X-ray and radio light curves of 1ES 1927+654 since 2021. The top panel shows the 0.3–2 keV flux (in units of 10^{-12} erg cm^{-2} s^{-1}) observed by the Swift/XRT (further details in S. Laha et al. 2024). The middle panel shows the total (log scale) VLBA/EVN flux in bands *C*, *X*, and *K* (5, 8.4, and 22.2/23.5 GHz, respectively), along with fluxes from lower-resolution AMI and e-MERLIN observations at 15.5 and 5 GHz, respectively. The bottom panel shows the evolution of the radio spectral index between 5 and 8.4 GHz (light red) and between 8.4 and 22 GHz (dark red); open circles denote two epochs of near-simultaneous observations for the lower band index. While the X-rays have shown considerable variability during the years since the late 2017 CL event, the radio remained quiescent in all bands until exhibiting an exponential rise over a few months in early 2023. The radio evolution since has shown only mild variability at or slightly below the peak radio flux density reached in 2023 June, with the exception of *K* band.

almost identical flux value to that of 2024 and is not shown). Both the submillimeter band SMA 225–345 GHz spectral index ($\alpha = 0.1 \pm 0.6$) and that between 23.6 and 225 GHz ($\alpha = 0.58 \pm 0.28$) suggest spectral hardening compared to the much steeper spectrum at the same epoch measured between 8.4 and 23.6 GHz ($\alpha = 1.05 \pm 0.26$). While the SMA observations are much lower in resolution and could include a contribution from arcsecond-scale emission (i.e., cold dust), the nearly flat submillimeter spectrum is consistent with the observations and expectations of synchrotron emission from a compact corona (e.g., I. Raginski & A. Laor 2016) rather than the Rayleigh–Jeans tail of a cold dust component. Additional higher-frequency observations should help clarify the degree of jet contribution to the SMA band and better constrain a possible turnover above 300 GHz.

3.2. Extended Source Structure and Proper Motion

VLBA imaging of 1ES 1927+654 has previously shown a low-level resolved component on scales of approximately a few parsecs with a typical flux of no more than a few millijanskys. As previously presented in S. Laha et al. 2022, the *C*-band (5.4 GHz) VLBA image of the source taken in 2021 March shows a central peak of approximately 2 mJy beam^{-1}, while the total flux is 5.5 ± 0.5 mJy (indicating a resolved component). Fitting of the visibilities with a modified version of DIFMAP (M. C. Shepherd et al. 1994; A. Roychowdhury 2023) showed that the extended flux was consistent with a disklike component of uniform surface brightness (total flux $\sim$4 mJy) and a size of 3.5×4.5 mas^2 (1.3×1.7 pc^2). Similar results for the peak and extended component were obtained for the 2022 March and August

observations, with some hints of a reduction in the disk size (by ∼20%) in the latter epoch (R. Ghosh et al. 2023). Surprisingly, the extended component was not detected at all (size < 0.1 pc, flux < 0.1 mJy) at *C* band by 2023 April 27, when the unresolved core had begun to rise. It is possible that this emission arose from the slowly expanding result of a previous outburst that became optically thin and went below the level of detection by early 2023; unfortunately, we lack multiband observations from that time for a more clear spectral analysis.

While a detailed investigation of the source structure through visibility fitting of all VLBA epochs (as well as simulations to better estimate the dominant systematic contribution to the errors) is deferred to a future publication, we show in Figure 4 core-subtracted *K*-band VLBA images from 2023 June 8 at 22.2 GHz (epoch BM549D) and 2024 February 9, April 24, and May 30 at 23.6 GHz. The 2024 February observation is deeper owing to combining the allotted time of two observations from a nominally monthly monitoring program (7 hr vs. 3.5 hr scheduling block), while the May observation was augmented to make a 6.2 hr scheduling block; the UV coverage in February and May is therefore better than in April, and this is likely the reason for the larger errors on component fits for the April epoch.

After core subtraction, two peaks on opposite sides of the core are apparent in the residual images. A robust kinematic analysis is not possible at this time, due to the limited number of epochs available, but we do report the results from directly fitting the visibilities for the 2024 February, April, and May *K*-band images in Table 2, with the caveat that the errors are underestimated owing to unaccounted-for systematic effects (see, e.g., A. B. Pushkarev et al. 2012).[32] The components were fit as point sources using the DIFMAP package, and the resulting flux density and position relative to the core are given in Columns (4)–(6). In Column (7) we give the total distance from the core position and the associated position angle from the core.

While the fits appear to suggest both increasing flux and separation in the resolved components (equivalent to an apparent separation speed of $0.36c$, or half that for a one-sided jet), we again urge caution owing to the underestimated errors, until more epochs of observation become available. Taking the mean separation of the components (0.45 mas) and assuming that the outflow began with the onset of the radio flare in 2023 February (14-month time baseline) also yields a similar separation speed estimate, of $0.38c$. Additional epochs of observation with good UV coverage are needed to confirm these initial estimates. Interestingly, the above speed estimates match the outflow speed (of $0.2c$) inferred from the 1 keV emission line seen during the super-Eddington state of 2020–2021—a time when radio observations were unfortunately lacking (M. Masterson et al. 2022). If the extended resolved features represent a jet-driven outflow, continued observations of the source should more clearly resolve these components with time.

[32] Estimates of the systematic contribution to the error require either extensive simulations of the data or time to accumulate many additional epochs of observation—both will be presented in a future paper. The EVN *K*-band observations, though reaching comparable theoretical sensitivity to the VLBA owing to long total observing times, lack the short-timescale SNR required for self-calibration and have large gaps in UV coverage on the scale of the extended components and therefore do not detect them. However, 1ES 1927+654 is approved for continued VLBA monitoring with deeper K-band observations through 2025.

The orientation of 1ES 1927+654 has not been clearly determined, starting from its early designation as a "naked" or true type 2 AGN (T. Boller et al. 2003), where the lack of obscuration seemed to point to an unusually underluminous broad-line region rather than greater obscuration consistent with standard AGN unification. Arguments have been made for both large (e.g., ∼85° based on Compton reflection model fits as in L. C. Gallo et al. 2013) and small orientation angles (e.g., B. Trakhtenbrot et al. 2019). The flux and speed of the bipolar outflow components detected in VLBI imaging can in principle constrain the orientation angle of the AGN, assuming that the jet/outflow is perpendicular to the disk and intrinsically symmetric in properties (see discussion and equations in, e.g., E. T. Meyer et al. 2018). While additional epochs are needed to provide a robust orientation estimate, the flux ratio of the jet/counterjet of ∼1 in combination with the low but still mildly relativistic apparent advance speed can at least rule out an orientation angle $\lesssim 20°$.

3.3. Source of the Radio Emission

Radio emission in radio-quiet AGNs can arise from a number of sources, including star formation and shocks from AGN-driven winds, small-scale jets, and/or the same compact corona that gives rise to X-ray emission (see, e.g., F. Panessa et al. 2019, for a recent review). In 1ES 1927+654, the first two origins can be ruled out easily based on both variability and physical scale. Indeed, comparison of low-resolution VLA and AMI observations taken at the same time as our VLBA observations shows no significant difference in total flux as might be expected if radio emission on larger scales (which would be resolved out by the VLBA) were significant. A strictly coronal origin for the gigahertz band compact emission is also precluded based on the requirements inferred from the X-ray observations (S. Laha et al. 2024), i.e., the very small size ($\sim 10 r_g$) and high magnetic field strength (on the order of 10^4–10^5 G). Besides very strong synchrotron self-absorption (SSA), which would be expected in such a source, there will be no significant synchrotron emission below the cyclotron frequency of $\sim(30\,\mathrm{GHz})(B/1 \times 10^4\,\mathrm{G})$.

A small-scale synchrotron jet/outflow[33] thus appears most consistent with the radio emission, even before the recent radio outburst. In this case the unresolved radio emission we observe arises on much larger scales than the X-ray-emitting corona. Taking a flux of 45 mJy at 15 GHz and radio spectral index $\alpha = 1$ as typical values since the flare began and assuming a source size of 0.05 pc, a minimum Lorentz factor $\gamma = 1$, and no beaming, we use the minimum-energy condition (equipartition) to derive a magnetic field for an emitting region of $B = 0.3$ G (standard formulae can be found in, e.g., M. S. Longair 2011).

For a synchrotron origin, the lack of polarization for 1ES 1927+654 in the 5 GHz VLA observation does not necessarily cause a problem, since internal Faraday depolarization is expected at the self-absorption frequency unless the plasma is dominated by highly relativistic electrons, with a lower-bound cutoff of $\gamma_{\rm min} \sim 10^2$ (T. W. Jones & S. L. O'Dell 1977), as is likely the case in more powerful jets (i.e., blazars). Indeed, high rotation measures and low observed radio polarization are typical of GPS sources (C. P. O'Dea 1998).

[33] In this Letter we use the terms "jet" and "outflow" interchangeably with regard to the resolved emission without intending them to represent different scenarios.

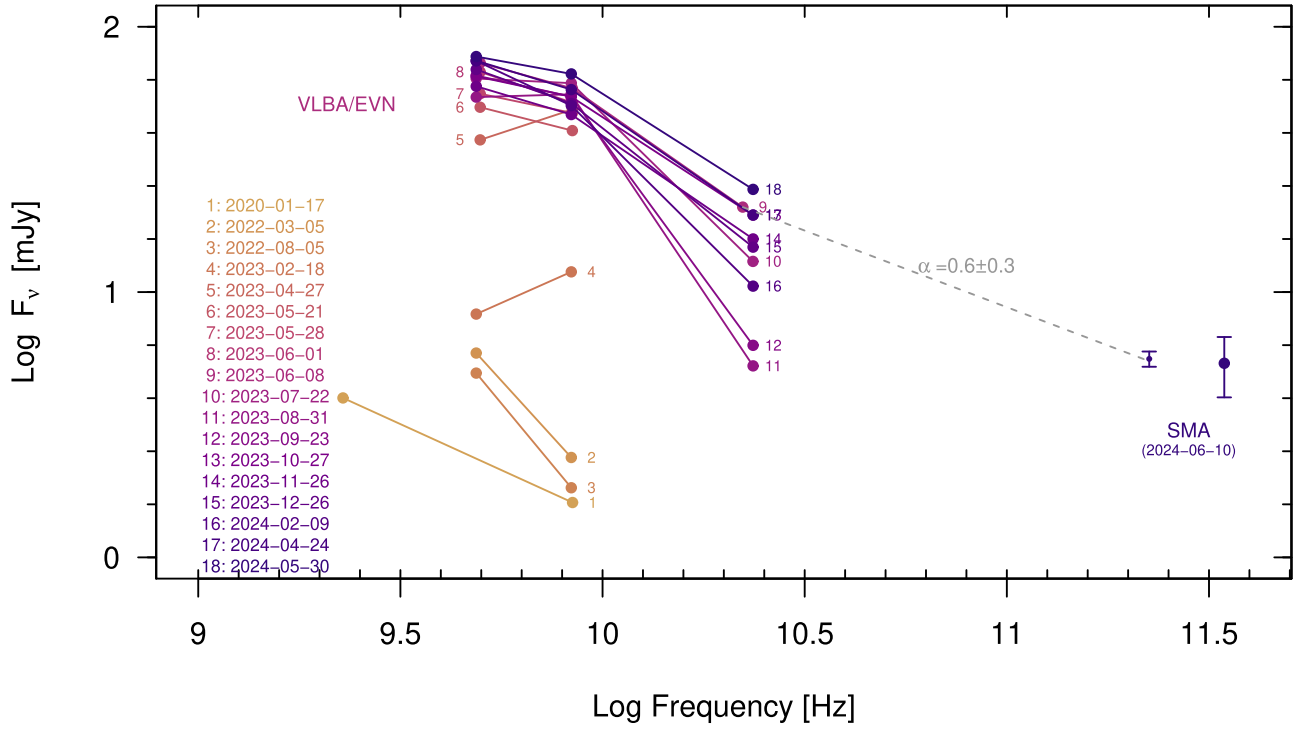

Figure 3. Plots of the radio spectral energy distribution (VLBI and SMA only), from 2020 January through 2024 April. As shown, the source exhibited a flat/hard spectrum during the initial rise in early 2023, but since then it shows a fairly consistent GPS. The peak of the spectrum appears to be at or just below 5 GHz. The SMA observations shown were taken on 2024 June 10 at 225 and 345 GHz and suggest a flat spectrum ($\alpha = 0.1 \pm 0.6$) in the submillimeter band, possibly consistent with a coronal origin. The 225 GHz flux in 2024 June is consistent with the value obtained in 2023 July at the same frequency.

While a full exploration of the X-ray and other multi-wavelength observations of this source are given in the companion publication by S. Laha et al. (2024), we can make some brief comments here. While a significant rise in the (0.3–2 keV) soft X-ray band is apparent in Figure 2, the hard X-rays have risen only slightly by a factor of perhaps 2–3, and the hardness ratio is now less than half of what it was before the soft X-ray rise. Similarly, the X-ray spectral index went from typical values of 2.6–2.8 prior to the radio flare to 3.2–3.3 after. The soft X-ray emission can be fit with a thermal component with a consistently low temperature (regardless of normalization) of $kT = 0.13$–0.16 keV.

Interpreting these observations, we first note that the X-ray to radio luminosity (10^4) is far too high for both to arise from nonthermal processes in a very compact jet (i.e., inverse Compton emission) as is likely occurring in compact symmetric objects (CSOs; M. Sobolewska et al. 2023), which this source otherwise resembles. Using the equipartition value of the magnetic field and assuming a "light" jet (electron–positron) and a subrelativistic speed of $0.3c$, we estimate a minimum total kinetic power for the jet of $L_{\rm kin,min} = 10^{43}\,{\rm erg\,s^{-1}}$, which is comparable to the observed power radiated in soft X-rays as of mid-2024. (Here we use $L_{\rm kin,min} = \pi R^2(\Gamma^2\beta)c\,U_B$ with $U_B = 0.0045\,{\rm erg\,cm^{-3}}$, $\Gamma^2\beta \approx 1$.) The onset of the soft X-ray rise just before the radio, as well as the spectral shape in the soft X-rays, could be consistent with shocked gas being driven by the newly launched radio jets, as an alternative to a coronal origin. In either case, assuming that the X-ray emission and radio emission are related, the delay in the radio emission could be explained by the presence of screening material causing free–free absorption; alternatively, the jet/outflow may be either too compact or simply inefficient at particle acceleration in the initial phase. If there is an external screen of hot gas, it must be on a larger scale than the jet-heated gas, on the order of the size of the broad-line region (30 lt-days or 0.25 pc), to account for the ∼200-day delay (see S. Laha et al. 2024).

3.4. Comparison with Young/Short-lived Jet Classes

As noted, the current spectrum of 1ES 1927+654 bears a resemblance to GPS sources, which are young radio jets less than 1000 yr old and usually <1 kpc in extent (e.g., C. P. O'Dea & D. J. Saikia 2021). The compact radio emission is due to synchrotron, with the characteristic gigahertz-frequency peak due to SSA or free–free absorption. The advance speeds of these jets are typically low, on the order of $0.1c$–$0.2c$. A related class of sources are known as CSOs, which are double-lobed radio sources <1 kpc in extent (A. C. S. Readhead et al. 1994, 1996). Unlike GPS sources, the CSO class is primarily a morphological one and requires high-resolution radio imaging for identification. They are often similarly identified as young radio sources $\lesssim$1000 yr in age and have relatively slow rates of growth in size, of $\sim 0.3c$ on average (G. B. Taylor et al. 2000; T. An & W. A. Baan 2012). In terms of their radio spectra, most CSO sources (e.g., 82% in the study of S. E. Tremblay et al. 2016) exhibit a GPS-like spectrum and can be core or lobe dominated (type 1 or 2, respectively). Very recent work on the kinematics of a carefully selected sample of mostly type 2 CSOs suggests that they should be considered a distinct class of "short-lived" jets rather than simply young versions of more classical powerful radio-loud AGNs (S. Kiehlmann et al. 2024). This fits well with the idea that CSO-type jet activity is powered by a "single fueling event," e.g., the disruption of a single star by the central BH

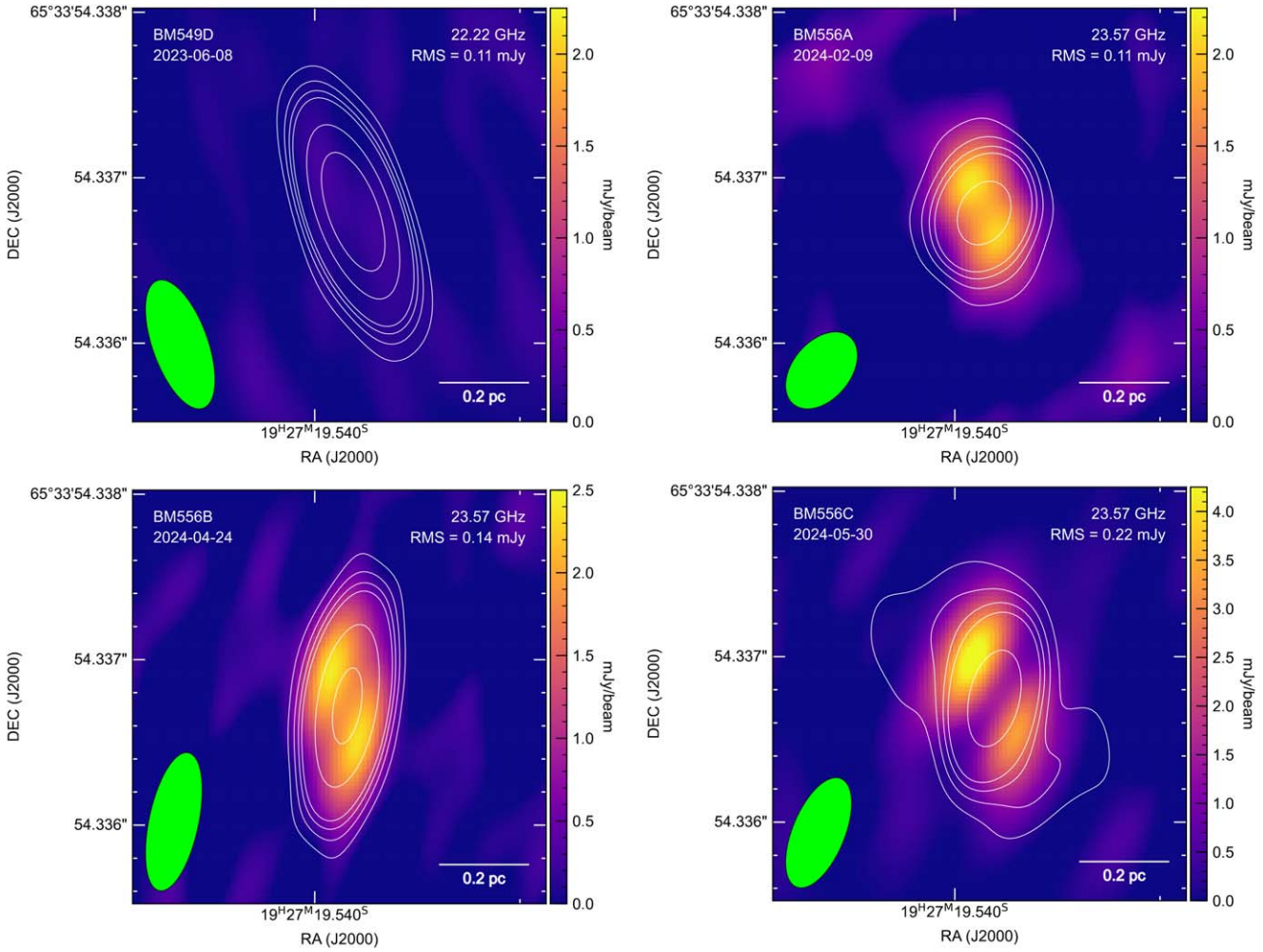

Figure 4. Core-subtracted *K*-band VLBA images of 1ES 1927+654 on 2023 June 8 (top left) 2024 February 9 (top right), 2024 April 24 (bottom left), and 2024 May 30 (bottom right). The contours correspond to the non-core-subtracted intensity and are drawn at 5, 10, 15, 20, and 50 times the non-core-subtracted image rms (given in the upper right corner of each panel). The longer 2024 February observation resulted in better UV coverage and a less elongated synthesized beam (green oval in the lower left corner of each panel) than the other observations. The extended structure apparent in early- to mid-2024 is entirely absent at the time of the initial radio outburst in 2023 June.

(A. C. S. Readhead et al. 1994; T. An & W. A. Baan 2012; S. Kiehlmann et al. 2024).

Although direct evidence of newly formed radio jets in AGNs is rare, it is not unprecedented. A recent study comparing the VLA All-Sky Survey (VLASS) epoch 1 observations (2017–2019) to the earlier Faint Images of the Radio Sky at Twenty cm (FIRST; 1993–2011) survey discovered 14 new radio-loud sources that have turned on sometime in the past ∼20 yr, and these also have peaked radio spectra resembling GPS sources (K. Nyland et al. 2020). The radio emission was roughly constant on few-month timescales on VLA follow-up, and the typically tens-of-gigahertz frequencies of the radio spectral peaks appear consistent with the expected size−peak frequency relation of young jets (C. P. O'Dea 1998; S. Jeyakumar 2016). The same is not true of 1ES 1927+654, where we clearly see that the spectral peak is below 5 GHz, contrary to expectations for a very young jet. On the other hand, its low luminosity does match its small size (<1 pc) according to the CSO luminosity-size relation, see e.g. Figure 1 of A. C. S. Readhead et al. (2024), where where only one other CSO is within an order of magnitude of the very low ($\sim 10^{22}$ W Hz^{-1}) radio luminosity of 1ES 1927+654.

While there is clear similarity between the case of 1ES 1927+654 and known young/short-lived jets, the radio powers of classical CSO and GPS sources are generally much higher than that of 1ES 1927+654, by a factor of >100 (C. P. O'Dea 1998; C. P. O'Dea & D. J. Saikia 2021). Even for the recently discovered VLASS sources, which extend down to lower radio power ($L_{3\mathrm{GHz}} = 40.5$ erg s^{-1}) than classical GPS samples, the lowest is still an order of magnitude more powerful in the radio than 1ES 1927+654. However, this may simply reflect the "down-sized" nature of 1ES 1927+654, which likely hosts a central BH of only $\sim 10^6\,M_\odot$ (R. Li et al. 2022). While there are some indications that GPS sources have somewhat smaller BH masses on average than their classical radio-loud QSO cousins (e.g., M. F. Gu et al. 2009; Q. Wu 2009), typical values are on the order of $M_{\mathrm{BH}} \sim 10^8\,M_\odot$, or 100× that of 1ES 1927+654. It is plausible that the lack of lower-power CSO sources in our current samples may simply be a selection effect. Indeed, although focusing on the far more prevalent non-CSO jet classes, the LOFAR Two-Metre Sky Survey found that the morphological class of edge-brightened (FR II) type jets, for decades thought to occur only at relatively high luminosities, actually extend down to luminosities 3 orders of magnitude below the traditional Fanaroff & Riley division (B. Mingo et al.

2019). As CSO sources appear to be relatively rare (6%–8%) in radio-selected AGN samples, and since only recently have moderately sized complete samples been compiled (e.g., 79 sources in S. Kiehlmann et al. 2024), deeper surveys may well uncover more objects like 1ES 1927+654.

3.5. Comparison to Late-time Radio Flares in TDEs

One observation that bears further exploration is the initial exponential rise in radio flux for 1ES 1927+654, which is in contrast with the prediction of a much slower $P \propto t^{2/5}$ behavior predicted for the turn-on of GPS sources (T. An & W. A. Baan 2012). Fast-rising radio brightening has been seen in TDEs, however (e.g., Y. Cendes et al. 2022), and the possibility that the 2017–2018 flare event in 1ES 1927+654 was a TDE is still open (C. Ricci et al. 2021). TDEs in existing AGNs are theoretically expected (e.g., C.-H. Chan et al. 2019) but are challenging to convincingly detect owing to competition from normal AGN flares (e.g., K. Auchettl et al. 2018). Interestingly, some recent theoretical work has suggested that TDEs in existing AGNs may precipitate CL events (Y. Wang et al. 2024).

TDEs are seen to produce prompt radio emission (within ∼100 days) in only about 20%–30% of cases. The radio is typically attributed to synchrotron emission from the interaction of outflows with circumnuclear material, as well as shocks formed in debris–stream collisions or, more rarely, relativistic jets (see K. D. Alexander et al. 2020, for a recent review). However, very recent work shows that late-time radio activity actually occurs in >40% of TDEs with initial nondetections or low-level detections (lower limit being due to limited follow-up), with onset times ranging from a few hundred to >1000 days (Y. Cendes et al. 2024, and references therein). These can exhibit very fast rise timescales, e.g., faster than $F_\nu \propto t^5$ in AT2018hyz (Y. Cendes et al. 2022). The latter case may be consistent with an off-axis relativistic jet, where the radio emission is initially "beamed away" before the jet decelerates enough to become visible (I. Sfaradi et al. 2023; but see also Y. Cendes et al. 2022). However, misaligned jets cannot explain the majority of cases, most directly because of the high rate of on-axis jetted TDE implied, which is not observed, and also because a decelerating jet scenario typically predicts a radio peak on the order of 100 days after onset, far less than the observed value of $\gtrsim$700 days (P. Beniamini et al. 2023; Y. Cendes et al. 2024; T. Matsumoto & T. Piran 2023). The origin of the probable outflows responsible for late-time radio emission in TDE is still under discussion; however, T. Matsumoto & T. Piran (2024) are able to explain delays up to those observed ($\sim 10^3$ days) as a natural consequence of nonrelativistic to very mildly relativistic outflows ($\beta < 0.15$) and the effects of a flattening density profile of the circumnuclear material.

The case of 1ES 1927+654 does show some similarities to TDEs with late-time radio emission. The timescale is only slightly longer than the most delayed onset in TDEs seen so far (at ∼1800 days), though one of the key conclusions of the recent discovery of late-time emission is that further long-term follow-up, possibly on decade timescales, is needed to fully characterize the phenomenon (Y. Cendes et al. 2024). K. D. Alexander et al. (2020) also note that a significant outflow may only be launched after (and if) the accretion onto the BH reaches a super-Eddington phase. For 1ES 1927+654 the time delay of the radio onset from its superluminal period in 2020 is ∼1000 days.

If our initial estimate of an outflow of speed $\sim 0.3c$ stands, then the outflow in 1ES 1927+654 is in an interesting middle regime between the subrelativistic outflows inferred in the sample of late-time TDE radio sources and the relativistic jets seen in small fractions of both AGNs and TDEs. The radio luminosity of 1ES 1927+654 is comparable to or slightly above the upper end of what is seen for nonrelativistic TDE outflows (typically $<10^{39}$ erg s^{-1}) but well below that of most radio-loud AGNs or, e.g., the famous jetted TDE Swift J1644+57 (E. Berger et al. 2012).

The BH mass of 1ES 1927+654 may explain some of the similarity in energy scale, as the BH masses for TDEs tend to be substantially smaller than in AGNs on average (e.g., 5×10^5–$10^7\, M_\odot$ in the sample of T. Ryu et al. 2020), reflecting the population of quiescent BHs and the fact that disruption events around BHs larger than $\sim 10^8\, M_\odot$ do not produce observable radiation. However, a down-sized BH does not mean that highly relativistic jets cannot form, as clearly demonstrated by the recent discoveries of relativistic, gamma-ray-emitting jets in narrow-line Seyfert galaxies (e.g., L. Foschini et al. 2015), as well as low-power but highly collimated/fast FR II jets, mentioned previously (B. Mingo et al. 2019). It seems likely that the difference comes down to the nature of jet launching itself, and further study of sources like 1ES 1927+654 will be key to advancing our understanding.

4. Conclusions

A little over 5 yr after it became one of extremely few AGNs with a directly observed CL event (B. Trakhtenbrot et al. 2019), 1ES 1927+654 has recently exhibited a significant radio brightening consistent with a newly launched radio-emitting outflow, approximately 1800 days after the initial CL event. A fortuitously timed weekly VLBA monitoring program in 2023 May–June caught the exponential rise and peak of the radio onset, which reached a level of 40 and 60 times previous radio core luminosities at 5 and 8.4 GHz, respectively. The source has maintained a relatively steady radio emission with a spectrum reminiscent of gigahertz-peaked sources for over 1 yr without obvious signs of fading or further increase. The soft X-ray emission, which began rising a few months prior to the flare, may arise from shock-heated gas impacted by the jet; in this scenario the radio jet may have been first screened by larger-scale and preexisting hot gas before breaking through, consistent with the delayed but rapid radio brightening. Our most recent high-resolution VLBA imaging at 23.6 GHz shows bipolar radio extensions of similar brightness separated by approximately 0.45 mas or 0.15 pc, with a tentative expansion of separation speed of $\sim 0.3c$. The resolved structures resemble very low luminosity CSOs, which have recently been suggested to be powered by TDE events (A. C. S. Readhead et al. 2024). The radio outflow characteristics also bear some resemblance to those TDEs with late-time radio emission, though, as noted in previous works, the X-ray properties of this source are considerably different from a TDE, likely due to the presence of a preexisting accretion disk. Continued follow-up with high-resolution and multifrequency radio observations will allow us to further constrain the kinematics and energetics of the outflow in this ever-changing and unique AGN.

Acknowledgments

E.T.M., O.S., and S.L. acknowledge support from NSF grant 2407801. F.P. acknowledges financial support from the Bando Ricerca Fondamentale INAF 2023. M.N. is supported by the European Research Council (ERC) under the European Union's Horizon 2020 research and innovation program (grant agreement No. 948381 948381) and by UK Space Agency grant No. ST/Y000692/1. The National Radio Astronomy Observatory is a facility of the National Science Foundation operated under cooperative agreement by Associated Universities, Inc. This work made use of the Swinburne University of Technology software correlator, developed as part of the Australian Major National Research Facilities Programme and operated under licence. e-MERLIN is a National Facility operated by the University of Manchester at Jodrell Bank Observatory on behalf of STFC, part of UK Research and Innovation. We thank the Mullard Radio Astronomy Observatory staff for the AMI observations. We acknowledge Phil Cigan and the MultiColorFits package, which was used to create the image figures (P. Cigan 2019). The Submillimeter Array is a joint project between the Smithsonian Astrophysical Observatory and the Academia Sinica Institute of Astronomy and Astrophysics and is funded by the Smithsonian Institution and the Academia Sinica. Maunakea, the location of the SMA, is a culturally important site for the indigenous Hawaiian people; we are privileged to study the cosmos from near its summit. Based on observations obtained with the Samuel Oschin Telescope 48 inch and the 60 inch Telescope at the Palomar Observatory as part of the Zwicky Transient Facility project. ZTF is supported by the National Science Foundation under grant No. AST-2034437 and a collaboration including Caltech, IPAC, the Weizmann Institute for Science, the Oskar Klein Center at Stockholm University, the University of Maryland, Deutsches Elektronen-Synchrotron and Humboldt University, the TANGO Consortium of Taiwan, the University of Wisconsin at Milwaukee, Trinity College Dublin, Lawrence Livermore National Laboratories, and IN2P3, France. Operations are conducted by COO, IPAC, and UW.

Facilities: VLA, VLBA, EVN, AMI, MERLIN, SMA, Swift.

ORCID iDs

Eileen T. Meyer https://orcid.org/0000-0002-7676-9962
Sibasish Laha https://orcid.org/0000-0003-2714-0487
Onic I. Shuvo https://orcid.org/0000-0003-4727-2209
Agniva Roychowdhury https://orcid.org/0000-0003-1101-8436
David A. Green https://orcid.org/0000-0003-3189-9998
Lauren Rhodes https://orcid.org/0000-0003-2705-4941
Amelia M. Hankla https://orcid.org/0000-0001-9725-5509
Alexander Philippov https://orcid.org/0000-0001-7801-0362
Rostom Mbarek https://orcid.org/0000-0001-9475-5292
Ari laor https://orcid.org/0000-0002-1615-179X
Mitchell C. Begelman https://orcid.org/0000-0003-0936-8488
Ritesh Ghosh https://orcid.org/0000-0003-4790-2653
Gabriele Bruni https://orcid.org/0000-0002-5182-6289
Francesca Panessa https://orcid.org/0000-0003-0543-3617
Matteo Guainazzi https://orcid.org/0000-0002-1094-3147
Ehud Behar https://orcid.org/0000-0001-9735-4873
Megan Masterson https://orcid.org/0000-0003-4127-0739
Haocheng Zhang https://orcid.org/0000-0001-9826-1759
Xiaolong Yang https://orcid.org/0000-0002-4439-5580
Mark A. Gurwell https://orcid.org/0000-0003-0685-3621
Garrett K. Keating https://orcid.org/0000-0002-3490-146X
David Williams-Baldwin https://orcid.org/0000-0001-7361-0246
Justin D. Bray https://orcid.org/0000-0002-0963-0223
Emmanuel K. Bempong-Manful https://orcid.org/0000-0002-1727-1224
Stefano Bianchi https://orcid.org/0000-0002-4622-4240
Federica Ricci https://orcid.org/0000-0001-5742-5980
Fabio La Franca https://orcid.org/0000-0002-1239-2721
Erin Kara https://orcid.org/0000-0003-0172-0854
Markos Georganopoulos https://orcid.org/0000-0002-2040-8666
Samantha Oates https://orcid.org/0000-0000-0000-0000
Matt Nicholl https://orcid.org/0000-0002-2555-3192
Main Pal https://orcid.org/0000-0001-6523-6522
S. Bradley Cenko https://orcid.org/0000-0003-1673-970X

References

Alexander, K. D., van Velzen, S., Horesh, A., & Zauderer, B. A. 2020, SSRv, 216, 81
Almeida, C. R., & Ricci, C. 2017, NatAs, 1, 679
An, T., & Baan, W. A. 2012, ApJ, 760, 77
Antonucci, R. 1993, ARA&A, 31, 473
Auchettl, K., Ramirez-Ruiz, E., & Guillochon, J. 2018, ApJ, 852, 37
Beniamini, P., Piran, T., & Matsumoto, T. 2023, MNRAS, 524, 1386
Berger, E., Zauderer, A., Pooley, G. G., et al. 2012, ApJ, 748, 36
Bianchi, S., Maiolino, R., & Risaliti, G. 2012, AdAst, 2012, 782030
Boller, T., Voges, W., Dennefeld, M., et al. 2003, A&A, 397, 557
CASA Team, Bean, B., Bhatnagar, S., et al. 2022, PASP, 134, 114501
Cendes, Y., Berger, E., Alexander, K. D., et al. 2022, ApJ, 938, 28
Cendes, Y., Berger, E., Alexander, K. D., et al. 2024, ApJ, 971, 185
Chan, C.-H., Piran, T., Krolik, J. H., & Saban, D. 2019, ApJ, 881, 113
Cigan, P., 2019 MultiColorFits: Colorize and Combine Multiple Fits Images for Visually Aesthetic Scientific Plots, Astrophysics Source Code Library, ascl:1909.002
Falcke, H., Sherwood, W., & Patnaik, A. R. 1996, ApJ, 471, 106
Foschini, L., Berton, M., Caccianiga, A., et al. 2015, A&A, 575, A13
Gallo, L. C., MacMackin, C., Vasudevan, R., et al. 2013, MNRAS, 433, 421
Ghosh, R., Laha, S., Meyer, E., et al. 2023, ApJ, 955, 3
Gu, M. F., Pak, S., & Ho, L. C. 2009, AN, 330, 253
Hickish, J., Razavi-Ghods, N., Perrott, Y. C., et al. 2018, MNRAS, 475, 5677
Janssen, M., Goddi, C., van Bemmel, I. M., et al. 2019, A&A, 626, A75
Jeyakumar, S. 2016, MNRAS, 458, 3786
Jones, T. W., & O'Dell, S. L. 1977, ApJ, 214, 522
Kiehlmann, S., Lister, M. L., Readhead, A. C. S., et al. 2024, ApJ, 961, 240
Kiehlmann, S., Readhead, A. C. S., O'Neill, S., et al. 2024, ApJ, 961, 241
Kokubo, M., & Minezaki, T. 2020, MNRAS, 491, 4615
Komossa, S., Grupe, D., Gallo, L. C., et al. 2020, A&A, 643, L7
Laha, S., Meyer, E., Roychowdhury, A., et al. 2022, ApJ, 931, 5
Laha, S., Meyer, E., Roychowdhury, A., et al. 2024, ApJ, submitted
Li, R., Ho, L. C., Ricci, C., et al. 2022, ApJ, 933, 70
Longair, M. S. 2011, High Energy Astrophysics (Cambridge: Cambridge Univ. Press)
Masci, F. J., Laher, R. R., Rusholme, B., et al. 2019, PASP, 131, 018003
Masterson, M., Kara, E., Ricci, C., et al. 2022, ApJ, 934, 35
Mathur, S., Denney, K. D., Gupta, A., et al. 2018, ApJ, 866, 123
Matsumoto, T., & Piran, T. 2023, MNRAS, 522, 4565
Matsumoto, T., & Piran, T. 2024, ApJ, 971, 49
Meyer, E. T., Petropoulou, M., Georganopoulos, M., et al. 2018, ApJ, 860, 9
Mingo, B., Croston, J. H., Hardcastle, M. J., et al. 2019, MNRAS, 488, 2701
Nicholls, B., Brimacombe, J., Kiyota, S., et al. 2018, ATel, 11391, 1
Nyland, K., Dong, D. Z., Patil, P., et al. 2020, ApJ, 905, 74
O'Dea, C. P. 1998, PASP, 110, 493
O'Dea, C. P., & Saikia, D. J. 2021, A&ARv, 29, 3
Panessa, F., Baldi, R. D., Laor, A., et al. 2019, NatAs, 3, 387
Perley, R. A., & Butler, B. J. 2017, ApJS, 230, 7
Perlman, E. S., Stocke, J. T., Schachter, J. F., et al. 1996, ApJS, 104, 251

Perrott, Y. C., Scaife, A. M. M., Green, D. A., et al. 2013, MNRAS, 429, 3330
Pushkarev, A. B., Hovatta, T., Kovalev, Y. Y., et al. 2012, A&A, 545, A113
Raginski, I., & Laor, A. 2016, MNRAS, 459, 2082
Readhead, A. C. S., Ravi, V., Blandford, R. D., et al. 2024, ApJ, 961, 242
Readhead, A. C. S., Taylor, G. B., Xu, W., et al. 1996, ApJ, 460, 612
Readhead, A. C. S., Xu, W., Pearson, T. J., Wilkinson, P. N., & Polatidis, A. G. 1994, in Compact Extragalactic Radio Sources, ed. J. A. Zensus & K. I. Kellermann (Green Bank, WV: National Radio Astronomy Observatory (NRAO)), 17
Ricci, C., Kara, E., Loewenstein, M., et al. 2020, ApJL, 898, L1
Ricci, C., Loewenstein, M., Kara, E., et al. 2021, ApJS, 255, 7
Ricci, C., & Trakhtenbrot, B. 2023, NatAs, 7, 1282
Roychowdhury, A. 2023, PhD Thesis, Univ. Maryland Baltimore County
Ryu, T., Krolik, J., & Piran, T. 2020, ApJ, 904, 73
Scepi, N., Begelman, M. C., & Dexter, J. 2021, MNRAS, 502, L50
Sfaradi, I., Beniamini, P., Horesh, A., et al. 2023, MNRAS, 527, 7672
Shappee, B. J., Prieto, J. L., Grupe, D., et al. 2014, ApJ, 788, 48
Shepherd, M. C. 1997, in ASP Conf. Ser. 125, Astronomical Data Analysis Software and Systems VI, ed. G. Hunt & H. Payne (San Francisco, CA: ASP), 77
Shepherd, M. C., Pearson, T. J., & Taylor, G. B. 1994, BAAS, 26, 987
Sobolewska, M., Siemiginowska, A., Migliori, G., et al. 2023, ApJ, 948, 81
Taylor, G. B., Marr, J. M., Pearson, T. J., & Readhead, A. C. S. 2000, ApJ, 541, 112
Tonry, J. L., Denneau, L., Heinze, A. N., et al. 2018, PASP, 130, 064505
Trakhtenbrot, B., Arcavi, I., MacLeod, C. L., et al. 2019, ApJ, 883, 94
Tran, H. D., Lyke, J. E., & Mader, J. A. 2011, ApJL, 726, L21
Tremblay, S. E., Taylor, G. B., Ortiz, A. A., et al. 2016, MNRAS, 459, 820
van Moorsel, G., Kemball, A., & Greisen, E. 1996, in ASP Conf. Ser. 101, Astronomical Data Analysis Software and Systems V, ed. G. H. Jacoby & J. Barnes (San Francisco, CA: ASP), 37
Wang, Y., Lin, D. N. C., Zhang, B., & Zhu, Z. 2024, ApJL, 962, L7
Wu, Q. 2009, MNRAS, 398, 1905
Zwart, J. T. L., Barker, R. W., Biddulph, P., et al. 2008, MNRAS, 391, 1545